ORIGINAL PAPER

Estimation of element-based zero-stress state for arterial FSI computations

**Kenji Takizawa · Hirokazu Takagi ·
Tayfun E. Tezduyar · Ryo Torii**

Abstract In patient-specific arterial fluid–structure inter-action (FSI) computations the image-based arterial geometry comes from a configuration that is not stress-free. We present a method for estimation of element-based zero-stress (ZS) state. The method has three main components. (1) An itera-tive method, which starts with an initial guess for the ZS state, is used for computing the element-based ZS state such that when a given pressure load is applied, the image-based target shape is matched. (2) A method for straight-tube geometries with single and multiple layers is used for computing the element-based ZS state so that we match the given diame-ter and longitudinal stretch in the target configuration and the "opening angle." (3) An element-based mapping between the arterial and straight-tube configurations is used for mapping from the arterial configuration to the straight-tube configu-ration, and for mapping the estimated ZS state of the straight tube back to the arterial configuration, to be used as the initial guess for the iterative method that matches the image-based target shape. We present a set of test computations to show how the method works.

K. Takizawa (✉) · H. Takagi
Department of Modern Mechanical Engineering and Waseda
Institute for Advanced Study, Waseda University, 1-6-1
Nishi-Waseda, Shinjuku-ku, Tokyo 169-8050, Japan
e-mail: Kenji.Takizawa@tafsm.org

T. E. Tezduyar
Mechanical Engineering, Rice University,
MS 321, 6100 Main Street, Houston, TX 77005, USA
e-mail: tezduyar@rice.edu

R. Torii
Department of Mechanical Engineering, University College London,
Torrington Place, London WC1E 7JE, UK

1 Introduction

Computational mechanics has been experiencing a rapid expansion in computational cardiovascular fluid mechanics (see, for example, [1–40]),with much emphasis on fluid–structure interaction (FSI) between the blood flow and car-diovascular wall. The expansion has partly been due to the advances in core FSI methods (see, for example, [36,37,41] and references therein) and the development of special meth-ods targeting cardiovascular FSI (see, for example, [29,33, 36] and references therein).

The special methods include those designed to take into account the fact that in patient-specific arterial FSI computa-tions the image-based arterial geometry comes from a con-figuration that is not stress-free. Until recently, no attempt was made to find a zero-stress (ZS) configuration for the artery. The concept of estimated zero-pressure (EZP) arterial geometry was introduced in [9]. It was pointed out in [9] that quite often, the image-based geometries were used as arter-ial geometries corresponding to zero blood pressure, and that it would be more realistic to use the image-based geometry as the arterial geometry corresponding to the time-averaged value of the blood pressure. Given that arterial geometry at the time-averaged pressure value, an estimated arterial geom-etry corresponding to zero blood pressure needed to be con-structed.

The original version of the technique for calculating an EZP geometry was introduced in a 2007 conference paper [42] and the 2008 journal paper [9] as "a rudimen-

tary technique" for addressing the issue. Newer techniques were introduced after that. They include the newer EZP versions introduced in [17,26,29], which were also presented in [33,36]. They also include the prestress technique introduced in [24] and further refined in [30], which also was presented in [33,36]. In the approach given in [24,30], a prestress state is found, which puts the artery in equilibrium with the time-averaged blood pressure (and viscous forces). The prestress is then directly employed for the arterial wall modeling in the FSI computations.

Arterial wall is a sophisticated multilayered composite with nonlinear stress–strain relationship. Moreover, because the arterial wall is a living tissue, its mechanical characteristics vary in time, and tissue growth over long time results in residual stress. A typical way to investigate the residual stress is to cut the arterial wall open and measure its "opening angle" [43–47]. Opening-angle measurements for various species were reported in [48]. The opening angle can then be used in the computations (see, for example, [49]) as part of the given data.

In this paper, we present a method for estimation of element-based ZS state. The method has three main components. The first component is an iterative method, which starts with an initial guess for the ZS state. It is used for computing the element-based ZS state such that when a given pressure load is applied, the image-based target shape is matched. The second component is a method for straight-tube geometries with single and multiple layers. It is used for computing the element-based ZS state so that we match the given diameter and longitudinal stretch in the target configuration and the opening angle. The third component is an element-based mapping between the arterial and straight-tube configurations. It is used for mapping from the arterial configuration to the straight-tube configuration, and for mapping the estimated ZS state of the straight tube back to the arterial configuration, to be used as the initial guess for the iterative method that matches the image-based target shape.

The first component is presented in Sect. 2. The second and third components are presented in Sect. 3. In Sect. 4, we present a set of test computations to show how the method works. The concluding remarks are given in Sect. 5.

2 Element-based zero-stress state

Let $\Omega_0 \in \mathbb{R}^3$ be the material domain of a structure in the ZS configuration, and let Γ_0 be its boundary. Let $\Omega_t \in \mathbb{R}^3$, $t \in (0, T)$, be the material domain of the structure in the deformed configuration, and let Γ_t be its boundary. The structural mechanics equations based on the total Lagrangian formulation can be written as

$$\int_{\Omega_0} \mathbf{w} \cdot \rho_0 \frac{\mathrm{d}^2 \mathbf{y}}{\mathrm{d}t^2}\, \mathrm{d}\Omega + \int_{\Omega_0} \delta \mathbf{E} : \mathbf{S}\, \mathrm{d}\Omega - \int_{\Omega_0} \mathbf{w} \cdot \rho_0 \mathbf{f}\, \mathrm{d}\Omega$$
$$= \int_{(\Gamma_t)_\mathrm{h}} \mathbf{w} \cdot \mathbf{h}\, \mathrm{d}\Gamma. \tag{1}$$

Here, $\mathbf{y}$ is the structural displacement, $\mathbf{w}$ is the virtual displacement, $\delta \mathbf{E}$ is the variation of the Green–Lagrange strain tensor, $\mathbf{S}$ is the second Piola–Kirchhoff stress tensor, ρ_0 is the mass density in the ZS configuration, $\mathbf{f}$ is the body force per unit mass, and $\mathbf{h}$ is the external traction vector applied on the subset $(\Gamma_t)_\mathrm{h}$ of the total boundary Γ_t.

2.1 Representation of the element-based ZS state

Typically the prestress is taken into account with the second Piola–Kirchhoff stress tensor as $\mathbf{S} + \mathbf{S}_0$. Applications in arterial FSI with prestress and a technique for finding the prestress can be found in [24,30]. Here, instead of finding a prestress, we look for a ZS shape, but for each element.

In the method we propose here, we define the ZS state with a set of positions $\mathbf{X}_0^e$ for each element e. Positions of nodes from different elements mapping to the same node in the mesh do not have to be the same. In the reference configuration, $\mathbf{X}_\mathrm{REF}$, all elements are connected by nodes, and we measure the displacement $\mathbf{y}$ from that connected configuration.

The implementation of this method is quite simple. The deformation gradient tensor $\mathbf{F}$ can be evaluated for each element:

$$\mathbf{F}^e \equiv \frac{\partial \mathbf{x}}{\partial \mathbf{X}_0^e}, \tag{2}$$
$$= \frac{\partial (\mathbf{X}_\mathrm{REF} + \mathbf{y})}{\partial \mathbf{X}_0^e}. \tag{3}$$

The deformation gradient tensors for different elements are on different configurations, but the terms in Eq. (1), including the second term, do not depend on the orientation. Therefore the rest of the process is the same as it is in the total Lagrangian formulation. We call this method the "element-based total Lagrangian (EBTL)" formulation.

2.2 An iterative method for finding the ZS state for a given load

One of the objectives of having prestress in arterial FSI computations is that we would like to have a configuration that matches the target shape under a given load. Here $\mathbf{X}_\mathrm{REF}$ represents the target shape. Suppose the element-based ZS state from the ith iteration is $(\mathbf{X}_0^e)^i$. We solve the steady-state structural mechanics equations with the EBTL formulation and obtain the displacement $\mathbf{y}^i$. If $\mathbf{y}^i$ is zero, then $(\mathbf{X}_0^e)^i$ is the converged solution. If not, then we follow the process below.

To explain the process, we first expand the definition of the deformation gradient tensor $\mathbf{F}$ to any two states $\mathbf{x}$ and $\mathbf{X}$, used as function arguments:

$$\mathbf{F}(\mathbf{x}, \mathbf{X}) = \frac{\partial \mathbf{x}}{\partial \mathbf{X}}. \tag{4}$$

We decompose this into rotation $\mathbf{R}$ and the right and left stretch tensors $\mathbf{U}$ and $\mathbf{V}$:

$$\mathbf{F}(\mathbf{x}, \mathbf{X}) = \mathbf{R}(\mathbf{x}, \mathbf{X})\,\mathbf{U}(\mathbf{x}, \mathbf{X}), \tag{5}$$

$$\mathbf{F}(\mathbf{x}, \mathbf{X}) = \mathbf{V}(\mathbf{x}, \mathbf{X})\,\mathbf{R}(\mathbf{x}, \mathbf{X}). \tag{6}$$

The decompositions can be obtained by using the following equations:

$$\mathbf{U}^2 = \mathbf{F}^T \mathbf{F}, \tag{7}$$

$$\mathbf{V}^2 = \mathbf{F} \mathbf{F}^T. \tag{8}$$

The relationship between the unit vectors $\mathbf{a}_0$ and $\mathbf{a}$ in the ZS and target configurations can be expressed as

$$\lambda_a \mathbf{a} = \mathbf{F} \mathbf{a}_0, \tag{9}$$

where λ_a is the stretch. Suppose we have the following relationship at ith iteration:

$$\lambda_a^i \mathbf{a}^i = \mathbf{F}^i \mathbf{a}_0^i, \tag{10}$$

where $\mathbf{a}_0^i$ is an arbitrary unit vector in $(\mathbf{X}_0^e)^i$, and

$$\mathbf{F}^i \equiv \mathbf{F}\left(\mathbf{x}^i, (\mathbf{X}_0^e)^i\right). \tag{11}$$

We also write a similar relationship between the next-iteration and target states $(\mathbf{X}_0^e)^{i+1}$ and $\mathbf{X}_{\mathrm{REF}}$:

$$\lambda_a \mathbf{a} = \mathbf{F}^{i+1} \mathbf{a}_0^{i+1}, \tag{12}$$

where $\mathbf{a}_0^{i+1}$ is an arbitrary unit vector in $(\mathbf{X}_0^e)^{i+1}$, and

$$\mathbf{F}^{i+1} \equiv \mathbf{F}\left(\mathbf{X}_{\mathrm{REF}}, (\mathbf{X}_0^e)^{i+1}\right). \tag{13}$$

Figure 1 shows the configurations we are working with.

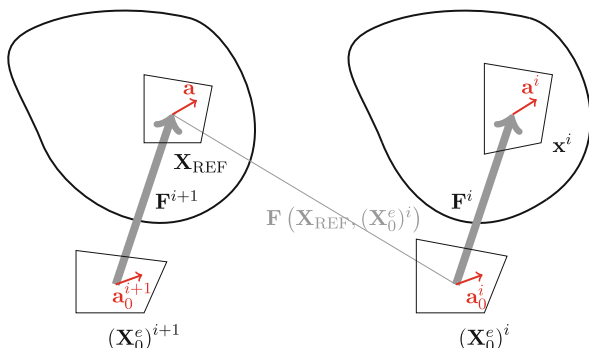Here we assume

$$\lambda_a = \lambda_a^i. \tag{14}$$

Fig. 1 Configurations we are working with

We write the relationship between the directions in $(\mathbf{X}_0^e)^{i+1}$ and $(\mathbf{X}_0^e)^i$ as follows:

$$\mathbf{a}_0^i = \mathbf{R}\left((\mathbf{X}_0^e)^i, (\mathbf{X}_0^e)^{i+1}\right) \mathbf{a}_0^{i+1}. \tag{15}$$

Now, we also assume that the direction we get from

$$\mathbf{a} = \mathbf{R}\left(\mathbf{X}_{\mathrm{REF}}, \mathbf{x}^i\right) \mathbf{a}^i \tag{16}$$

is the same as the direction given by Eq. (12). Substituting Eq. (15) into Eq. (10), premultiplying both sides by $\mathbf{R}\left(\mathbf{X}_{\mathrm{REF}}, \mathbf{x}^i\right)$, and using Eqs. (14) and (16), we get

$$\lambda_a \mathbf{a} = \mathbf{R}\left(\mathbf{X}_{\mathrm{REF}}, \mathbf{x}^i\right) \mathbf{F}^i \mathbf{R}\left((\mathbf{X}_0^e)^i, (\mathbf{X}_0^e)^{i+1}\right) \mathbf{a}_0^{i+1}. \tag{17}$$

Because $\mathbf{a}_0^{i+1}$ is an arbitrary vector, we obtain the following relationship from Eqs. (12) and (17):

$$\mathbf{F}^{i+1} = \mathbf{R}\left(\mathbf{X}_{\mathrm{REF}}, \mathbf{x}^i\right) \mathbf{F}^i \mathbf{R}\left((\mathbf{X}_0^e)^i, (\mathbf{X}_0^e)^{i+1}\right). \tag{18}$$

Now, we assume that the following approximation is a reasonable one:

$$\mathbf{R}\left((\mathbf{X}_0^e)^i, (\mathbf{X}_0^e)^{i+1}\right) = \mathbf{I}. \tag{19}$$

Thus,

$$\mathbf{F}^{i+1} = \mathbf{R}\left(\mathbf{X}_{\mathrm{REF}}, \mathbf{x}^i\right) \mathbf{F}^i, \tag{20}$$

and

$$\left(\mathbf{F}^{i+1}\right)^{-1} = \left(\mathbf{F}^i\right)^{-1} \mathbf{R}(\mathbf{x}^i, \mathbf{X}_{\mathrm{REF}}), \tag{21}$$

$$= \left(\mathbf{U}^i\right)^{-1} \mathbf{R}((\mathbf{X}_0^e)^i, \mathbf{X}_{\mathrm{REF}}). \tag{22}$$

With this tensor, we calculate $(\mathbf{X}_0^e)^{i+1}$ from the target state $\mathbf{X}_{\mathrm{REF}}$.

Remark 1 Inspecting $\mathbf{F}^{i+1}$, as obtained from Eq. (22):

$$\mathbf{F}^{i+1} = \mathbf{R}(\mathbf{X}_{\mathrm{REF}}, (\mathbf{X}_0^e)^i)\mathbf{U}(\mathbf{x}^i, (\mathbf{X}_0^e)^i), \tag{23}$$

we observe that the rotation is based on $(\mathbf{X}_0^e)^i$ and $\mathbf{X}_{\mathrm{REF}}$, but the stretch is based on $\mathbf{x}^i$ and $(\mathbf{X}_0^e)^i$.

In this paper we use hexahedral elements, and we evaluate the tensors at the element center. With that, we compute explicitly as follows:

$$(\mathbf{X}_0^e)_a^{i+1} - \overline{(\mathbf{X}_0^e)^{i+1}}$$
$$= \underbrace{\left(\overline{\mathbf{U}^{e^i}}\right)^{-1} \overline{\mathbf{R}^e}((\mathbf{X}_0^e)^i, \mathbf{X}_{\mathrm{REF}})}_{\mathbf{K}^i} \left((\mathbf{X}_{\mathrm{REF}}^e)_a - \overline{\mathbf{X}_{\mathrm{REF}}^e}\right), \tag{24}$$

with an overbar indicating the element-center value. What we see in Eq. (24) is that the ZS state is obtained using a transformation matrix $\mathbf{K}^i$, which gives us only six degrees of choice, from the target state, which is already set. To increase the degrees of choice, we propose an alternative method:

$$(\mathbf{X}_0^e)_a^{i+1} - \overline{(\mathbf{X}_0^e)^{i+1}}$$

$$= \underbrace{\mathbf{K}^i \overline{\mathbf{F}^e}(\mathbf{X}_{\text{REF}}, (\mathbf{X}_0^e)^i)}_{\hat{\mathbf{K}}^i} \left((\mathbf{X}_0^e)^i - \overline{(\mathbf{X}_0^e)^i} \right), \tag{25}$$

$$= \hat{\mathbf{K}}^i \hat{\mathbf{K}}^{i-1} \cdots \hat{\mathbf{K}}^1 \hat{\mathbf{K}}^0 \left((\mathbf{X}_0^e)_a^0 - \overline{(\mathbf{X}_0^e)^0} \right). \tag{26}$$

Again the ZS state is obtained using a transformation matrix, but from the initial guess for the ZS state, which gives us additional degrees of choice. We note that Eq. (26) is only for better understanding of the method, and we implement Eq. (25). We will call the iterations given by Eq. (24), with direct update from the target state, "direct-update (DU)" process, and the iterations given by Eq. (25), with recursive update from the previous iteration, "recursive-update (RU)" process. The RU process is our preferred method, and unless specified otherwise, that is what we use in the computations reported in this paper.

Remark 2 If we do not approximate Eq. (22) by using the element-center values, the two processes are identical.

3 Modeling of the ZS state for an artery

3.1 Tube shape

We describe a tube-shaped model in the target state with three lengths: $\overline{\ell}$, h and L. They are the circumferential length at the arterial-wall center, wall thickness, and the length in the longitudinal direction. The volume of the tube is

$$V = \overline{\ell} h L. \tag{27}$$

There are significant properties for an artery beyond having a target shape under a certain load. One of them is the opening angle, ϕ, seen after a longitudinal cut, which we call the "LC state."

Remark 3 We note that it is not necessary for the LC state to be a ZS state.

To describe the LC representation, we define ϕ as shown in Fig. 2. With that ϕ definition, the curvature can be written as follows:

$$\kappa = \frac{2\pi - \phi}{\ell_0}, \tag{28}$$

where the subscript 0 indicates a value at the LC state.

3.1.1 Single-layer model

In this model we assume that the LC state is a ZS state. The subscripts "I" and "E" indicate values corresponding to the internal (lumen) and external surfaces. The radii of curvature are given as follows:
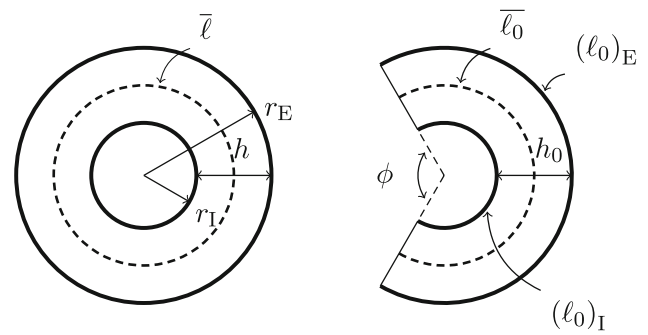

Fig. 2 Straight-tube (*left*) and opening-angle (*right*) definitions

$$(r_\text{I})_0 = \frac{(\ell_\text{I})_0}{|2\pi - \phi|}, \tag{29}$$

$$(r_\text{E})_0 = \frac{(\ell_\text{E})_0}{|2\pi - \phi|}, \tag{30}$$

and the thickness is

$$h_0 = |(r_\text{E})_0 - (r_\text{I})_0|. \tag{31}$$

Remark 4 We note that the expressions provided by Eqs. (29) and (30) give infinite radii for $\phi = 2\pi$.

The volume of the LC state is

$$V_0 = \frac{2\pi - \phi}{2} \left((r_\text{E})_0^2 - (r_\text{I})_0^2 \right) L_0, \tag{32}$$

$$= \frac{2\pi - \phi}{2} ((r_\text{E})_0 - (r_\text{I})_0) ((r_\text{E})_0 + (r_\text{I})_0) L_0, \tag{33}$$

$$= \overline{\ell_0} h_0 L_0, \tag{34}$$

where

$$\overline{\ell_0} = \frac{(\ell_\text{E})_0 + (\ell_\text{I})_0}{2}. \tag{35}$$

Remark 5 We note that the expression given by Eq. (34) is applicable also for $\phi = 2\pi$.

In the process of creating $\mathbf{X}_0^e$, ϕ is specified based on data, and the longitudinal stress, $\lambda_z = \frac{L}{L_0}$, is specified based on values from the literature. We iterate on the value of $\overline{\ell_0}$ to match $\overline{\ell}$ by solving the structural mechanics equations, and h_0 is a dependent parameter from the material incompressibility, which is enforced through Eqs. (27) and (34).

We introduce the parametric coordinate $-1 \leq \eta \leq 1$, and have the following linear relationship in the ZS state:

$$\ell_0(\eta) = (\ell_\text{I})_0 \frac{1 - \eta}{2} + (\ell_\text{E})_0 \frac{1 + \eta}{2}, \tag{36}$$

$$= \overline{\ell_0} + \frac{\Delta \ell_0}{2} \eta, \tag{37}$$

where

$$\Delta \ell_0 = (\ell_\text{E})_0 - (\ell_\text{I})_0, \tag{38}$$

$$= (2\pi - \phi) h_0. \tag{39}$$

From the material incompressibility we write

$$2\pi r \, \mathrm{d}r \, L = \ell_0 \mathrm{d}\eta \frac{h_0}{2} L_0. \tag{40}$$

Integrating both sides, we obtain

$$\pi \left(r^2 - r_{\mathrm{I}}^2\right) L = \frac{h_0}{2} L_0 \left(\overline{\ell_0}(\eta+1) + \frac{\Delta \ell_0}{4}\left(\eta^2 - 1\right)\right). \tag{41}$$

We solve this for η:

$$\eta = 2 \frac{\sqrt{\left(\overline{\ell_0} - \frac{\Delta \ell_0}{2}\right)^2 + \Delta \ell_0 \frac{2\pi \left(r^2 - r_{\mathrm{I}}^2\right) L}{h_0 L_0}} - \overline{\ell_0}}{\Delta \ell_0}, \tag{42}$$

$$= 2 \frac{-\overline{\ell_0} + \frac{\Delta \ell_0}{4} + \frac{2\pi \left(r^2 - r_{\mathrm{I}}^2\right) L}{h_0 L_0}}{\sqrt{\left(\overline{\ell_0} - \frac{\Delta \ell_0}{2}\right)^2 + \Delta \ell_0 \frac{2\pi \left(r^2 - r_{\mathrm{I}}^2\right) L}{h_0 L_0}} + \overline{\ell_0}}, \tag{43}$$

$$= 2 \frac{2 \frac{r^2 - r_{\mathrm{I}}^2}{r_{\mathrm{E}}^2 - r_{\mathrm{I}}^2} + \frac{\Delta \ell_0}{4 \overline{\ell_0}} - 1}{\sqrt{\left(1 - \frac{\Delta \ell_0}{2 \overline{\ell_0}}\right)^2 + 2 \frac{\Delta \ell_0}{\overline{\ell_0}} \frac{r^2 - r_{\mathrm{I}}^2}{r_{\mathrm{E}}^2 - r_{\mathrm{I}}^2} + 1}}. \tag{44}$$

Equation (44) is applicable also for $\phi = 2\pi$. We introduce $-\pi \le \theta \le \pi$ in the circumferential direction. Because of the circular symmetry in the deformed state, including the strain, the angle in the LC state can be written as

$$\theta_0 = \frac{2\pi - \phi}{2\pi} \theta. \tag{45}$$

We cannot use this expression for elements crossed by $\theta = \pm \pi$, and therefore we rearrange the mapping as

$$\theta_0^e = \frac{2\pi - \phi}{2\pi} \left(\theta - \overline{\theta^e}\right), \tag{46}$$

and that avoids $\theta = \pm \pi$ crossing the element. Here $\overline{\theta^e}$ is the angle for the element center.

With the parameter set (η, θ, z), we have the mapping

$$\mathbf{X}_0^e = \frac{h_0}{2}\eta \mathbf{e}_r(0) + \frac{\overline{\ell_0}}{2}\frac{\theta}{\pi}\mathbf{e}_\theta(0) + \frac{z}{\lambda_z}\mathbf{e}_z \tag{47}$$

for $\phi = 2\pi$, and otherwise

$$\mathbf{X}_0^e = \left(\frac{\overline{\ell_0}}{2\pi - \phi} + \frac{h_0}{2}\eta\right)\mathbf{e}_r\left(\theta_0^e\right)$$

$$- \left(\frac{\overline{\ell_0}}{2\pi - \phi}\right)\mathbf{e}_r(0) + \frac{z}{\lambda_z}\mathbf{e}_z, \tag{48}$$

$$= \frac{\overline{\ell_0}}{2\pi - \phi}\left(\mathbf{e}_r\left(\theta_0^e\right) - \mathbf{e}_r(0)\right)$$

$$+ \frac{h_0}{2}\eta \mathbf{e}_r\left(\theta_0^e\right) + \frac{z}{\lambda_z}\mathbf{e}_z. \tag{49}$$

Because Eq. (49) is not valid for $\phi \to 2\pi$, we rearrange the first term as

$$\frac{\overline{\ell_0}}{2\pi - \phi}\left(\mathbf{e}_r\left(\theta_0^e\right) - \mathbf{e}_r(0)\right) = \frac{\overline{\ell_0}}{2\pi - \phi}\begin{bmatrix} \cos\left(\theta_0^e\right) - 1 \\ \sin\left(\theta_0^e\right) \end{bmatrix}, \tag{50}$$

and approximate it by a Taylor series expansion:

$$\frac{\overline{\ell_0}}{2\pi - \phi}\left(\mathbf{e}_r\left(\theta_0^e\right) - \mathbf{e}_r(0)\right)$$

$$\approx \frac{\overline{\ell_0}}{2\pi - \phi}\begin{bmatrix} \left(\theta_0^e\right)^2 \left(-\frac{1}{2} + \frac{1}{24}\left(\theta_0^e\right)^2\right) \\ \theta_0^e\left(1 - \frac{1}{6}\left(\theta_0^e\right)^2\right) \end{bmatrix}$$

$$= \frac{\overline{\ell_0}}{2\pi}\left(\theta - \overline{\theta^e}\right)\begin{bmatrix} \theta_0^e\left(-\frac{1}{2} + \frac{1}{24}\left(\theta_0^e\right)^2\right) \\ \left(1 - \frac{1}{6}\left(\theta_0^e\right)^2\right) \end{bmatrix}. \tag{51}$$

This form is valid for $\phi = 2\pi$, and if $|\phi - 2\pi| < 2 \times 10^{-4}$, the error in the approximation is within 10^{-16}. Thus, Eq. (49) and its approximation by Eq. (51) can be used for creating $\mathbf{X}_0^e$.

3.1.2 Three-layer model

We extend the single-layer model to a three-layer model. We assume that the three layers are in a ZS state after they are separated. Then each layer has its own opening angle ϕ_i, and we can simply use the single-layer model to create $\mathbf{X}_0^e$. We also assume that the model has an opening angle ϕ in the LC state, prior to the separation of the three layers. However, this angle cannot be specified directly. It can be matched iteratively by introducing an angle $\overline{\phi}$, which is related, by Eq. (39), to $\Delta \ell_0$ indicated in Fig. 3. With that, we can calculate $\left(\overline{\ell_i}\right)_0$ as follows:
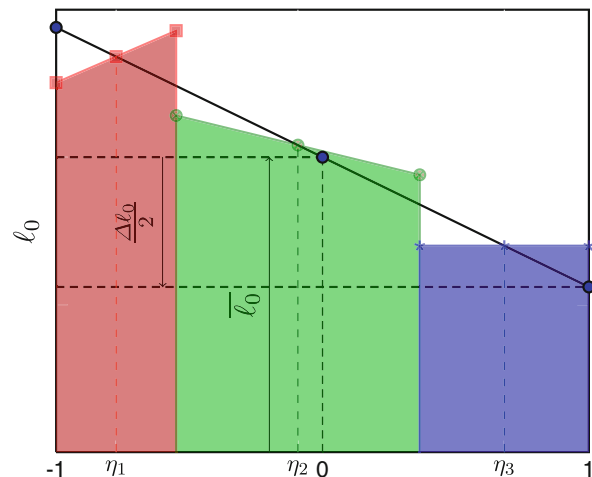

Fig. 3 Three-layer model. Circumferential length as function of η

$$\left(\overline{\ell_i}\right)_0 = \overline{\ell_0} + \frac{\Delta\ell_0}{2}\eta_i, \tag{52}$$

where η_i is the parametric coordinate of the center of the ith layer:

$$\eta_i = \frac{2}{h_0}\left(\sum_{k=1}^{i-1}(h_k)_0 + \frac{1}{2}(h_i)_0\right) - 1. \tag{53}$$

In the process of creating $\mathbf{X}_0^e$, $(\lambda_z)_i$ is specified as before, and ϕ_i and $\frac{(h_i)_0}{h_0}$ are also specified. We iterate on the values of $\overline{\ell_0}$ and $\overline{\phi}$ to match $\overline{\ell}$ and ϕ by solving the structural mechanics equations, and h_0 is again a dependent parameter. While this is now a two-dimensional search, we know that ϕ depends mostly on $\overline{\phi}$, and less on $\overline{\ell_0}$.

3.2 Arbitrary shape

We define centerlines for the artery. We can obtain the centerlines by using Vascular Modeling Toolkit [50]. A centerline consists of straight-line segments.

We first calculate the positions of the centerline nodes along the artery from the inlet, and this is the z-coordinate. We also introduce the basis vector $\mathbf{e}_r(0)$ orthogonal to the centerline, noting that the argument "0" is for $\theta = 0$.

We define the basis vectors from the inlet to the outlet sequentially. First we pick a basis vector at the inlet, and rotate it as we move along the centerline to make it perpendicular to the centerline segments.

With what we have from above, we define the following parameters for each element node: z, θ, r, $r_{\min}$, and $r_{\max}$. If there are branches, for each element we choose the closest one among the centerlines. We define $r_{\min}$ and $r_{\max}$ for each node as the coordinates of the closest internal and external surface positions, respectively. These are used for defining the mapped radius $\hat{r}$ as follows:

$$\hat{r} = r_I + \frac{r - r_{\min}}{r_{\max} - r_{\min}}(r_E - r_I), \tag{54}$$

where r_I and r_E are tube internal and external surface radii. These do not need to match $r_{\min}$ and $r_{\max}$. They are calculated from the centerline nodal values by interpolation at the projection point of the artery node. The centerline nodal values are calculated from the cross-sectional areas over planes orthogonal to the centerline at the centerline nodes. The orthogonality direction for a node is defined by averaging the orthogonality directions for the adjacent segments. With $\hat{r}$, we obtain the tube position $\mathbf{x}_T$ as follows:

$$\mathbf{x}_T = \hat{r}\mathbf{e}_r(\theta) + z\mathbf{e}_z. \tag{55}$$

To construct the ZS state, we use either the single-layer or three-layer model. For example, in the case of the single-layer model, we first choose ϕ and λ_z and find the proper $\overline{\ell_0}$ and h_0 from the straight-tube solution (described in Sect. 4),
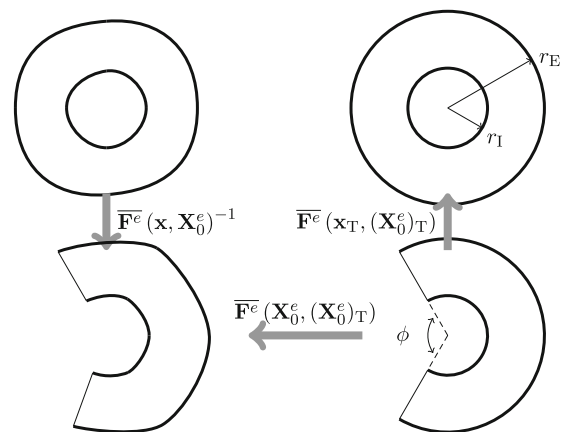

Fig. 4 Artery (*top left*), straight tube (*top right*), ZS state of the straight tube (*bottom right*), and ZS state of the artery (*bottom left*)
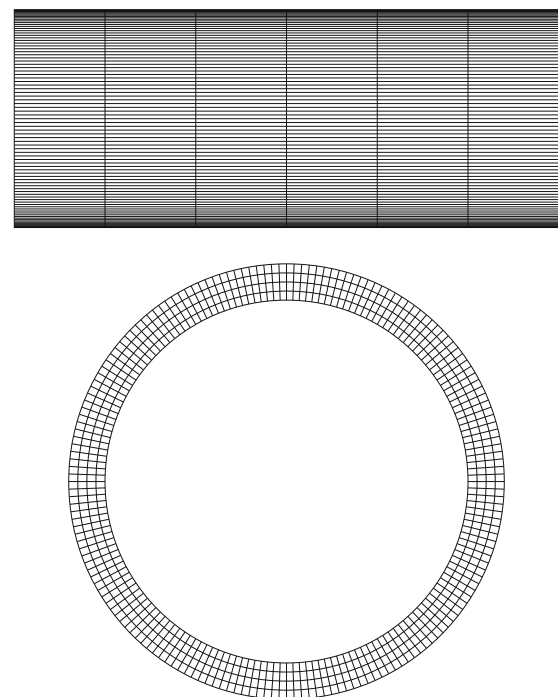

Fig. 5 Mesh for the single-layer model

then we map $\hat{r}$ to η by Eq. (44), and then we use Eq. (49) to obtain $(\mathbf{X}_0^e)_T$. After that, we pull $(\mathbf{X}_0^e)_T$ back onto the actual configuration with mappings similar to those in Sect. 2.2. Figure 4 shows the configurations of the process.

To pull $(\mathbf{X}_0^e)_T$ back, we again start with the following assumption:

$$\mathbf{F}\left(\mathbf{x}, (\mathbf{X}_0^e)\right) = \mathbf{R}(\mathbf{x}, \mathbf{x}_T)\,\mathbf{F}\left(\mathbf{x}_T, (\mathbf{X}_0^e)_T\right)\mathbf{R}\left((\mathbf{X}_0^e)_T, \mathbf{X}_0^e\right). \tag{56}$$

Then we obtain

$$\left(\mathbf{F}\left(\mathbf{x}, (\mathbf{X}_0^e)\right)\right)^{-1}$$
$$= \mathbf{R}\left(\mathbf{X}_0^e, (\mathbf{X}_0^e)_T\right)\left(\mathbf{F}\left(\mathbf{x}_T, (\mathbf{X}_0^e)_T\right)\right)^{-1}\mathbf{R}(\mathbf{x}_T, \mathbf{x}), \tag{57}$$

Table 1 Single-layer model. First two values of α and the number of binary-search iterations, n_b

ϕ	α^1	α^2	n_b
(a) $\lambda_z = 1.0$			
$13\pi/6$	0.8	0.85	6
$7\pi/3$	0.8	0.85	7
$5\pi/2$	0.8	0.85	7
$8\pi/3$	0.8	0.85	7
(b) $\lambda_z = 1.1$			
$13\pi/6$	0.9	0.95	6
$7\pi/3$	0.9	0.95	6
$5\pi/2$	0.9	0.95	7
$8\pi/3$	0.9	0.95	6
(c) $\lambda_z = 1.2$			
$13\pi/6$	1.0	1.05	5
$7\pi/3$	1.0	1.05	5
$5\pi/2$	1.0	1.05	5
$8\pi/3$	1.0	1.05	5
(d) $\lambda_z = 1.3$			
$13\pi/6$	1.1	1.15	4
$7\pi/3$	1.1	1.15	5
$5\pi/2$	1.1	1.15	5
$8\pi/3$	1.1	1.15	5
(e) $\lambda_z = 1.4$			
$13\pi/6$	1.2	1.25	5
$7\pi/3$	1.2	1.25	5
$5\pi/2$	1.2	1.25	5
$8\pi/3$	1.2	1.25	6
(f) $\lambda_z = 1.5$			
$13\pi/6$	1.3	1.35	6
$7\pi/3$	1.3	1.35	6
$5\pi/2$	1.3	1.35	6
$8\pi/3$	1.3	1.35	6

again assume $\mathbf{R}\left(\mathbf{X}_0^e, (\mathbf{X}_0^e)_T\right) = \mathbf{I}$, and obtain

$$\left(\mathbf{F}\left(\mathbf{x}, (\mathbf{X}_0^e)\right)\right)^{-1} = \left(\mathbf{F}\left(\mathbf{x}_T, (\mathbf{X}_0^e)_T\right)\right)^{-1} \mathbf{R}\left(\mathbf{x}_T, \mathbf{x}\right). \tag{58}$$

We obtain $(\mathbf{X}_0^e)_a$ from $\mathbf{x}_a^e$ as follows:

$$(\mathbf{X}_0^e)_a - \overline{\mathbf{X}_0^e} = \left(\overline{\mathbf{F}^e}\left(\mathbf{x}_T, (\mathbf{X}_0^e)_T\right)\right)^{-1} \overline{\mathbf{R}^e}\left(\mathbf{x}_T, \mathbf{x}\right)\left(\mathbf{x}_a^e - \overline{\mathbf{x}^e}\right). \tag{59}$$

An alternative way of obtaining $\mathbf{X}_0^e$ is using the following relationship:

$$\left(\mathbf{F}\left(\mathbf{x}, (\mathbf{X}_0^e)\right)\right)^{-1} \mathbf{F}\left(\mathbf{x}, (\mathbf{X}_0^e)_T\right)$$
$$= \left(\mathbf{F}\left(\mathbf{x}_T, (\mathbf{X}_0^e)_T\right)\right)^{-1} \mathbf{R}\left(\mathbf{x}_T, \mathbf{x}\right) \mathbf{F}\left(\mathbf{x}, (\mathbf{X}_0^e)_T\right), \tag{60}$$
$$\mathbf{F}\left((\mathbf{X}_0^e), (\mathbf{X}_0^e)_T\right)$$
$$= \mathbf{F}\left((\mathbf{X}_0^e)_T, \mathbf{x}_T\right) \mathbf{R}\left(\mathbf{x}_T, \mathbf{x}\right) \mathbf{F}\left(\mathbf{x}, (\mathbf{X}_0^e)_T\right), \tag{61}$$

$$= \mathbf{V}\left((\mathbf{X}_0^e)_T, \mathbf{x}_T\right) \mathbf{U}\left(\mathbf{x}, (\mathbf{X}_0^e)_T\right), \tag{62}$$

and calculating as follows:

$$(\mathbf{X}_0^e)_a - \overline{(\mathbf{X}_0^e)}$$
$$= \overline{\mathbf{V}^e}\left((\mathbf{X}_0^e)_T, \mathbf{x}_T\right) \overline{\mathbf{U}^e}\left(\mathbf{x}, (\mathbf{X}_0^e)_T\right)\left(((\mathbf{X}_0^e)_T)_a - \overline{((\mathbf{X}_0^e)_T)}\right). \tag{63}$$

We use $\mathbf{X}_0^e$ as the initial guess for the iterations described in Sect. 2.2. Our preferred mapping is the one given by Eq. (63), and that is what we use in the computations reported in this paper.

4 Test computations

The arterial wall is modeled with the continuum element made of hyperelastic (Fung) material. The Fung material constants D_1 and D_2 (from [51]) are 2.6447×10^3 N/m^2 and 8.365, and the penalty Poisson's ratio is 0.45. We set constant pressure $p_0 = 92$ mm Hg.

We use the steady-state formulation. The boundary condition at the tube ends is free displacement in the radial direction from the centroid of those ends.

4.1 Straight tube

The target artery shape has 10 % thickness ratio, $\pi h/\ell_I$, and longitudinal-length ratio $\pi L/\ell_I = 3$. We note that the solution depends on D_1/p_0 and the thickness ratio, but not on the diameter or the longitudinal-length ratio. For the test computations, we define a parameter α:

$$\overline{\ell_0} = \alpha \ell_I. \tag{64}$$

In the following test computations, we consider ϕ and λ_z as given. We assume the α that gives 10 % thickness ratio after the structural mechanics computation is the proper α. Based on this assumption, we iterate on α using a binary-search-like method. First we compute with two given α: α^1 and α^2, and update α with the formula

$$\alpha^{i+1} = \alpha^c + \frac{\alpha^+ - \alpha^-}{\ell_I^+ - \ell_I^-}\left(\ell_I - \ell_I^c\right), \tag{65}$$

where $-$ and $+$ indicate the solutions closest to ℓ_I approached from below and above among the set of all solutions, and c is the closest one among the two. When $\left|\alpha^c - \alpha^i\right| \leq 10^{-5}$, we consider the iterations converged.

Since we use a penalty form of the incompressibility constraint, we do not have the exact volume conservation. Therefore we adjust h_0 such that we have the correct volume at the target state. Within the iterations above, we adjust the thickness as follows:
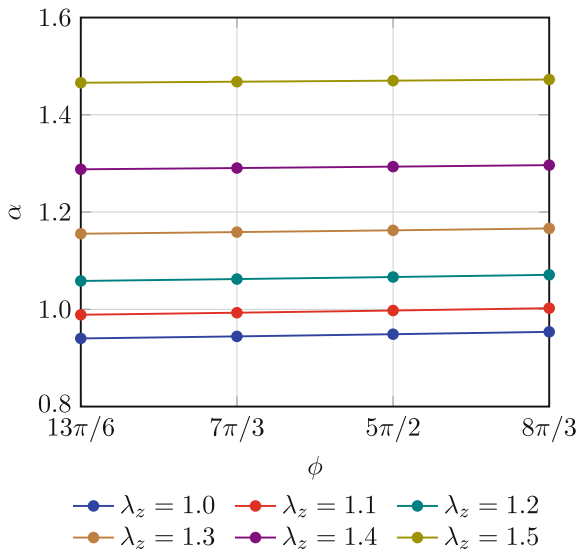
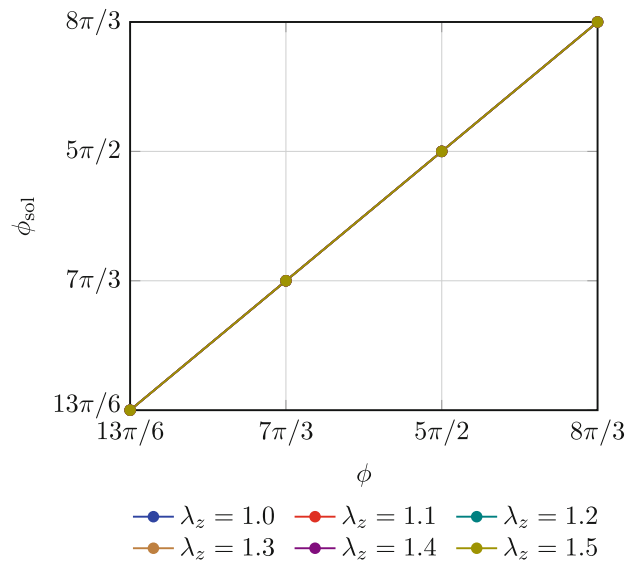**Fig. 6** Single-layer model. Converged values of α

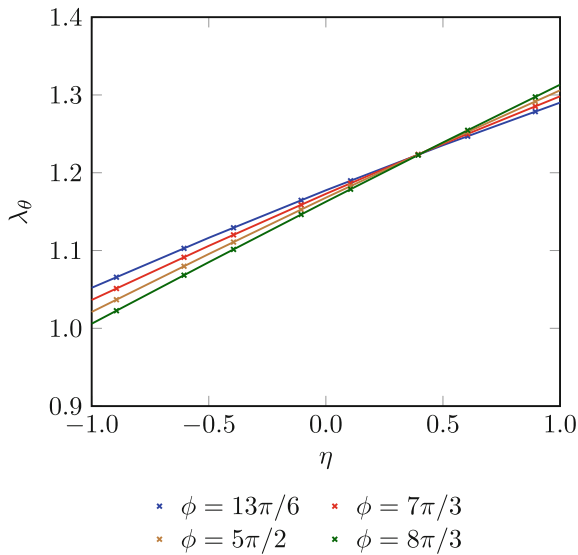**Fig. 8** Single-layer model. Actual cut angle, ϕ_{sol}

Fig. 7 Single-layer model. Circumferential prestretch introduced by the element-based ZS state for $\lambda_z = 1.0$. *Markers* are the integration-point values and the *curves* are after least-squares projection on to the nodes
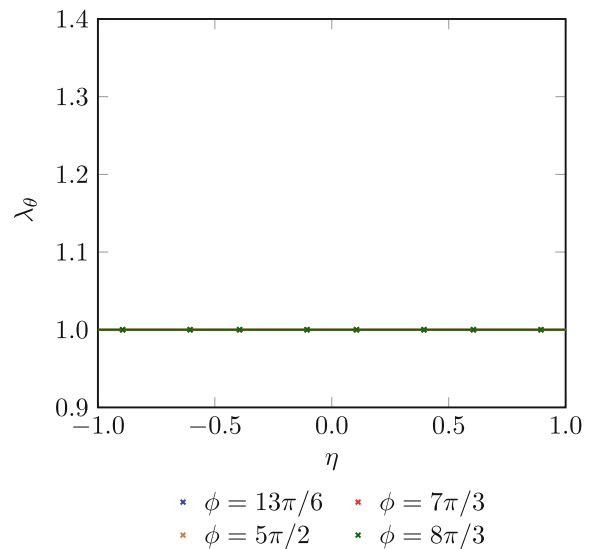

Fig. 9 Single-layer model. For the case $\lambda_z = 1.0$, circumferential stretch for the LC state

$$h_0^{j+1} = \frac{V}{V^j} h_0^j, \tag{66}$$

where V and V^j are the volumes of the target and the jth solution, respectively. The initial value of h_0 is set based on the volume conservation ($V_0 = V$) with Eq. (34), and we do this adjustment three times for each α^i.

In this paper, we present test computations for given values of $\phi = 13\pi/6$, $7\pi/3$, $5\pi/2$, and $8\pi/3$. For each opening angle, we consider $\lambda_z = \{1.0, 1.1, \ldots, 1.5\}$. So, we have a total of 24 test cases.

4.1.1 Single-layer model

The number of elements in the thickness, circumferential and longitudinal directions are 4, 180 and 6, respectively. The mesh is shown in Fig. 5. In solving the steady-state structural mechanics equations, the number of nonlinear iterations is 75, and the number of GMRES [52] iterations per nonlinear iteration is 200. The values of α^1 and α^2, and the number of binary-search iterations, n_b, are shown in Table 1.

Figure 6 shows the converged values of α. From Fig. 6, we can see that α has a rather weak dependence on ϕ, and it is determined almost entirely by λ_z. We represent the relationship between ϕ, λ_z and α with the following expression obtained by least-squares fit:

Table 2 Thickness ratios and opening angles. Figure 3 was generated from this data

i	ϕ_i	$(h_i)_0 / h_0$
1	$2\pi/9$	0.2252
2	3π	0.4572
3	2π	0.3176
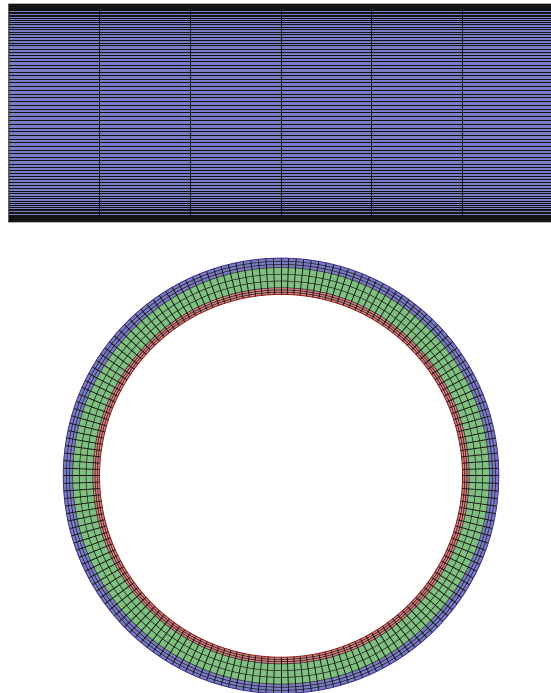
Fig. 10 Mesh for the three-layer model

$$\alpha = (0.011\phi + 1.887) \left(0.807\lambda_z^2 - 1.496\lambda_z + 1.171 \right). \quad (67)$$

Figure 7 shows the circumferential prestretch, λ_θ, introduced by the element-based ZS state. Figure 8 shows the actual cut angle, ϕ_{sol}, obtained from the computation based on the ZS state. It is clear that ϕ_{sol} is the same as the specified ϕ, and therefore the following relationship holds:

$$\phi_{\mathrm{sol}} = \phi. \quad (68)$$

Figure 9 shows, for the case $\lambda_z = 1.0$, the circumferential stretch for the LC state, and the constant value of 1.0 is also consistent with what we expect to see in the LC state. With Eqs. (67) and (68), we can model the ZS state for an arbitrary shape with single layer.

In solving the steady-state structural mechanics equations for the LC state, the number of nonlinear iterations is 200, and the number of GMRES iterations per nonlinear iterations is 1,000.

Table 3 Three-layer model. First two values of α and the number of binary-search iterations, n_{b}

$\overline{\phi}$	α^1	α^2	n_{b}
(a) $\lambda_z = 1.0$			
$13\pi/6$	0.9	1.0	5
$7\pi/3$	0.9	1.0	6
$5\pi/2$	0.9	1.0	7
$8\pi/3$	0.9	1.0	6
(b) $\lambda_z = 1.1$			
$13\pi/6$	1.0	1.1	5
$7\pi/3$	1.0	1.1	5
$5\pi/2$	1.0	1.1	5
$8\pi/3$	1.0	1.1	4
(c) $\lambda_z = 1.2$			
$13\pi/6$	1.05	1.15	5
$7\pi/3$	1.05	1.15	5
$5\pi/2$	1.05	1.15	5
$8\pi/3$	1.05	1.15	5
(d) $\lambda_z = 1.3$			
$13\pi/6$	1.1	1.2	5
$7\pi/3$	1.1	1.2	5
$5\pi/2$	1.1	1.2	6
$8\pi/3$	1.1	1.2	5
(e) $\lambda_z = 1.4$			
$13\pi/6$	1.2	1.3	5
$7\pi/3$	1.2	1.3	5
$5\pi/2$	1.2	1.3	5
$8\pi/3$	1.2	1.3	5
(f) $\lambda_z = 1.5$			
$13\pi/6$	1.3	1.4	6
$7\pi/3$	1.3	1.4	7
$5\pi/2$	1.3	1.4	6
$8\pi/3$	1.3	1.4	6

4.1.2 Three-layer model

To construct the three-layer model, we also need the thickness ratio and opening angle for each layer at the ZS state. We use experimental data [47] for that, which is shown in Table 2. The number of elements in the thickness, circumferential and longitudinal directions are 9, 180 and 6, respectively. The mesh is shown in Fig. 10.

Just like in the single-layer model, we iterate on α. In solving the steady-state structural mechanics equations, the number of nonlinear iterations is 100, and the number of GMRES iterations per nonlinear iteration is 200. The values of α^1, α^2 and n_{b} are shown in Table 3.

Figure 11 shows the converged values of α, and the prestretch is shown in Fig. 12. From Fig. 11, we can see that α is almost independent of $\overline{\phi}$, like in the single-layer model.
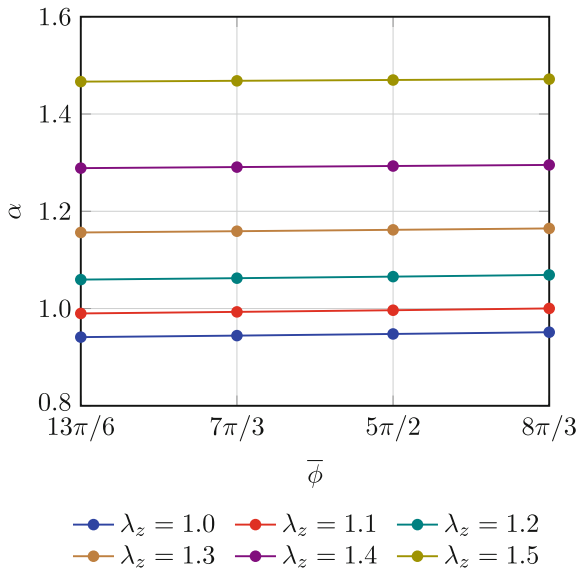
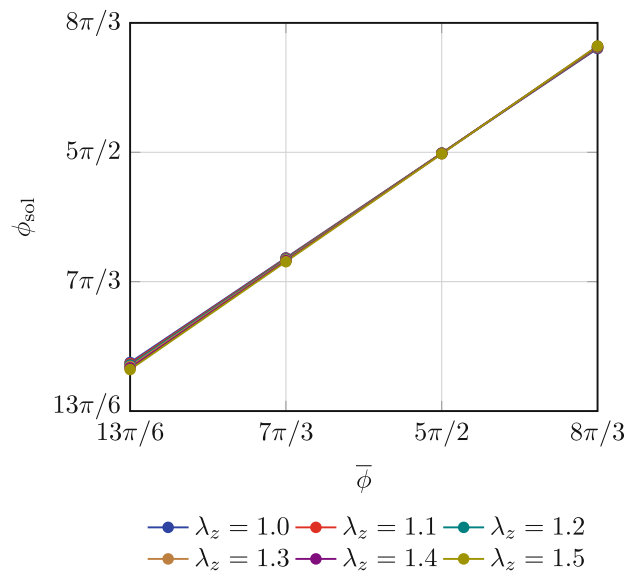Fig. 11 Three-layer model. Converged values of α

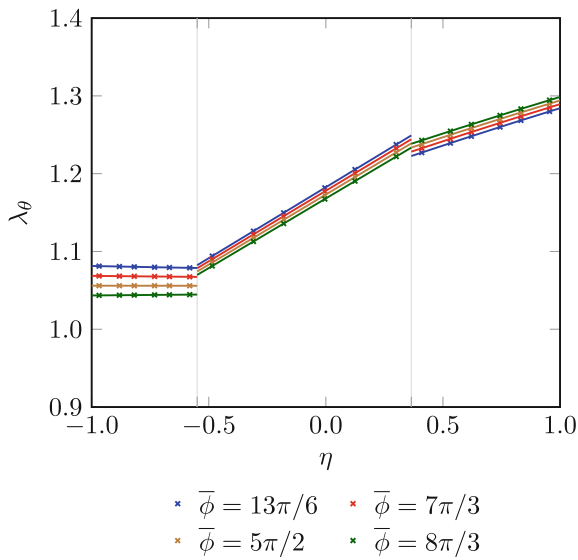

Fig. 13 Three-layer model. Actual cut angle, ϕ_{sol}

Fig. 12 Three-layer model. Circumferential prestretch introduced by the element-based ZS state for $\lambda_z = 1.0$. *Markers* are the integration-point values and the *curves* are after least-squares projection on to the nodes
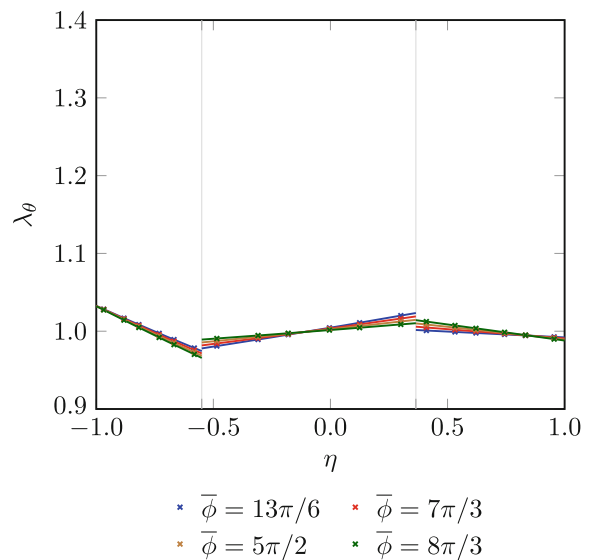
We represent the relationship between $\overline{\phi}$, λ_z and α with the following least-squares fit:

$$\alpha = \left(0.008\overline{\phi} + 1.897\right)\left(0.811\lambda_z^2 - 1.503\lambda_z + 1.176\right). \quad (69)$$

As we can see, Eqs. (67) and (69) are very close. Figure 13 shows the actual cut angle obtained from the computation based on the ZS state. As expected, ϕ_{sol} is not equal to $\overline{\phi}$. We represent the relationship between $\overline{\phi}$, λ_z and ϕ_{sol} with the following least-squares fit:

$$\phi_{sol} = \left(\overline{\phi} - 7.968\right)\left(0.049\lambda_z + 0.759\right) + 7.943. \quad (70)$$

Fig. 14 Three-layer model. For the case $\lambda_z = 1.0$, circumferential stretch in the LC state

Figure 14 shows, for the case $\lambda_z = 1.0$, the circumferential stretch for the LC state. With Eqs. (69) and (70), we can model the ZS state for an arbitrary shape with three layers.

In solving the steady-state structural mechanics equations for the LC states with three layers, the number of nonlinear iterations is 300, and the number of GMRES iterations per nonlinear iterations is 1,000.

4.2 Arbitrary shape: a curved tube

We use a curved-tube shape as the target shape, shown in Fig. 15. The tube is based on 1/12 of a torus with radius of
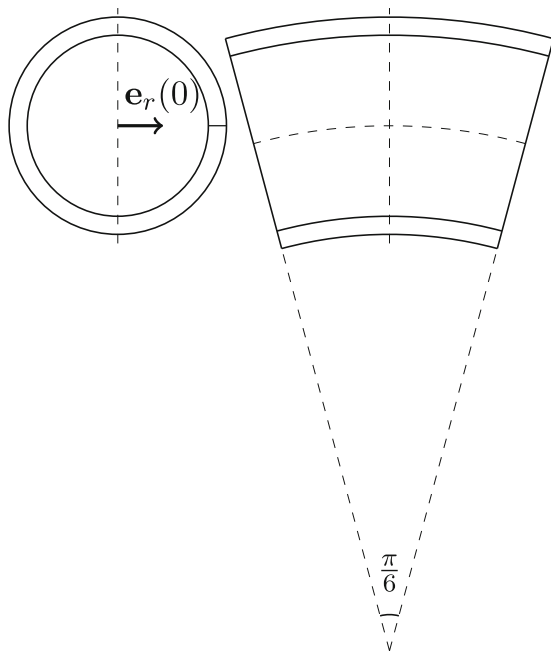
Fig. 15 A curved tube. Cross-sectional views at the tube center (*left*) and perpendicular to $\mathbf{e}_r(0)$ (*right*)

Table 4 A curved tube. Number of iterations to obtain $\mathbf{X}_0^e$

	$\lambda_z = 1.0$	$\lambda_z = 1.2$
$\phi = \pi/2$	16	13
$\phi = 5\pi/2$	19	13

curvature $5.8\ r_{\mathrm{I}}$. The resulting length along the centerline is $L = 3.037\ r_{\mathrm{I}}$. The thickness ratio is 10 %.

To obtain the ZS shape, we use the single-layer model and the results obtained in Sect. 4.1.1. For given ϕ and λ_z, we use Eq. (67) to obtain α, and then obtain $\overline{\ell_0}$ by Eq. (64).
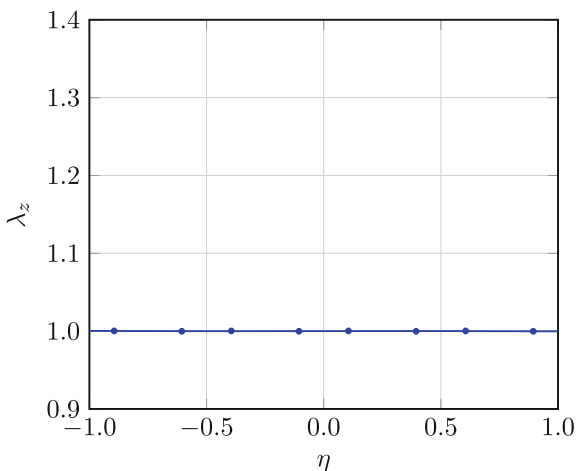
Fig. 16 A curved tube. For the case $\phi = \pi/2$ and $\lambda_z = 1.0$, the longitudinal prestretch introduced by $(\mathbf{X}_0^e)^0$
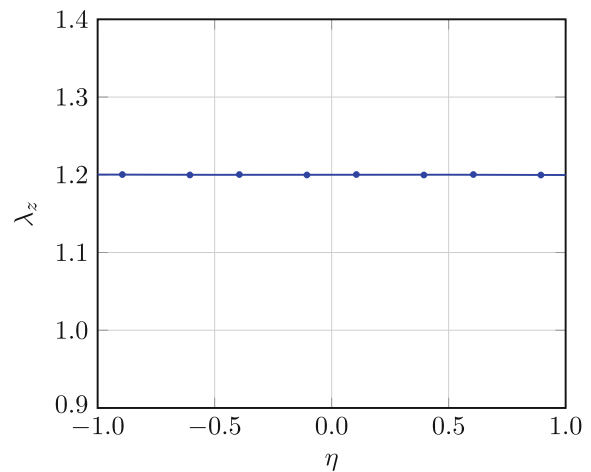
Fig. 17 A curved tube. For the case $\phi = \pi/2$ and $\lambda_z = 1.2$, the longitudinal prestretch introduced by $(\mathbf{X}_0^e)^0$
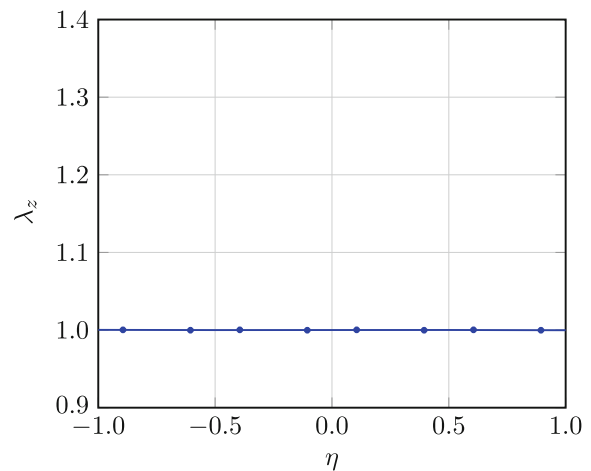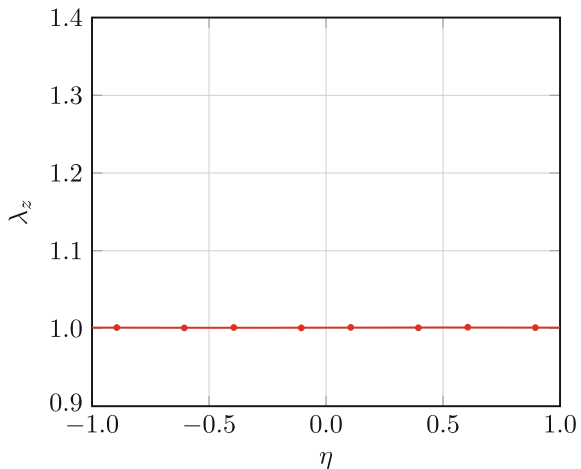

Fig. 18 A curved tube. For the case $\phi = 5\pi/2$ and $\lambda_z = 1.0$, the longitudinal prestretch introduced by $(\mathbf{X}_0^e)^0$
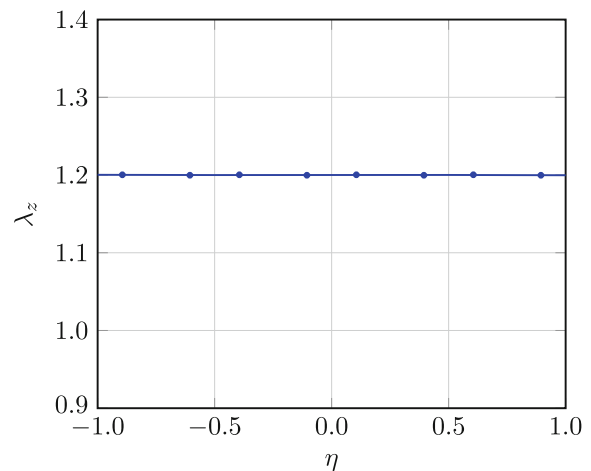
Fig. 19 A curved tube. For the case $\phi = 5\pi/2$ and $\lambda_z = 1.2$, the longitudinal prestretch introduced by $(\mathbf{X}_0^e)^0$
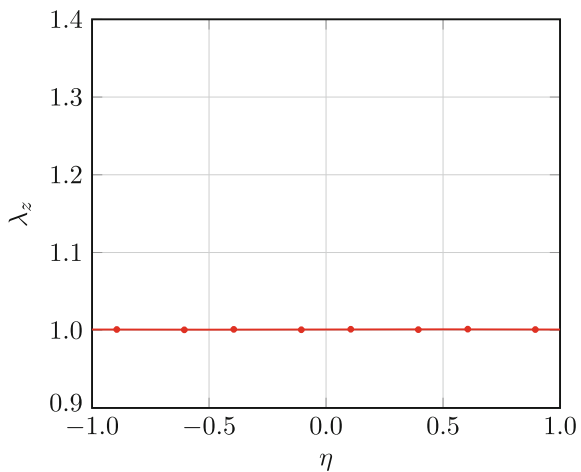
Fig. 20 A curved tube. For the case $\phi = \pi/2$ and $\lambda_z = 1.0$, the longitudinal prestretch introduced by $\mathbf{X}_0^e$
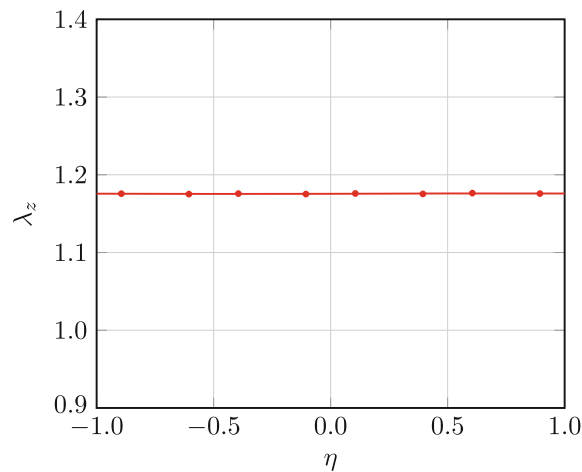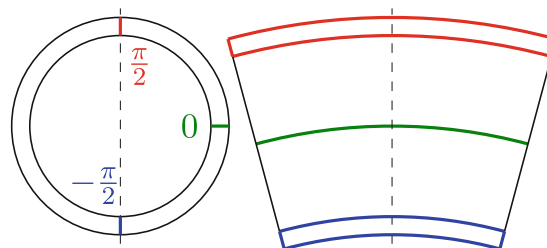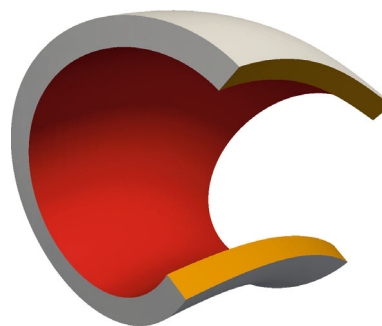

Fig. 23 A curved tube. For the case $\phi = 5\pi/2$ and $\lambda_z = 1.2$, the longitudinal prestretch introduced by $\mathbf{X}_0^e$
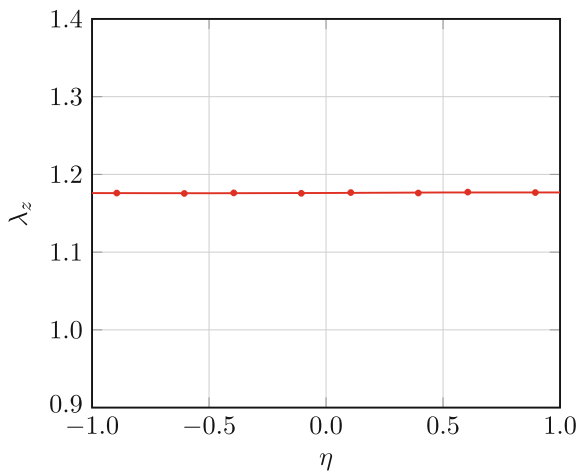
Fig. 21 A curved tube. For the case $\phi = \pi/2$ and $\lambda_z = 1.2$, the longitudinal prestretch introduced by $\mathbf{X}_0^e$

Fig. 24 A curved tube. Cutting locations $\theta_c = -\pi/2, 0, \pi/2$

Fig. 25 A curved tube. LC state for the case $\phi = \pi/2$ and $\lambda_z = 1.0$. The lumen is colored *red*, and the cut edge, $\theta_c = 0$, *orange*. (Color figure online)

We choose the basis vector $\mathbf{e}_r(0)$ as shown in Fig. 15, and it is constant along z in the tube coordinates system.

We have a total of 4 test cases; $\phi = \{\pi/2, 5\pi/2\}$ and $\lambda_z = \{1.0, 1.2\}$. The mesh consists of 14,400 hexahedral elements with 18,900 nodes. The number of elements in the thickness, circumferential and longitudinal directions are 4, 180 and 20, respectively.

4.2.1 ZS state

With the initial ZS state $(\mathbf{X}_0^e)^0$, we iterate using the method described in Sect. 2.2, until the L_2 norm$\|\mathbf{y}/r_I\|$ is less than
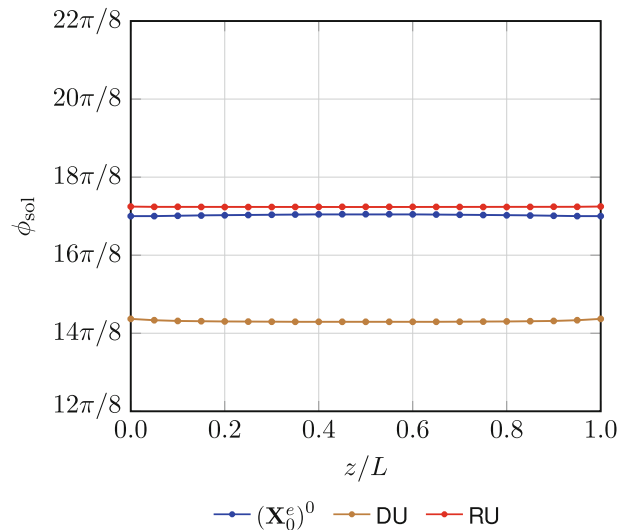

Fig. 22 A curved tube.For the case $\phi = 5\pi/2$ and $\lambda_z = 1.0$, the longitudinal prestretch introduced by $\mathbf{X}_0^e$

Fig. 26 A curved tube. LC state for the case $\phi = 5\pi/2$ and $\lambda_z = 1.0$. The lumen is colored *red*, and the cut edge, $\theta_c = 0$, *orange*. (Color figure online)
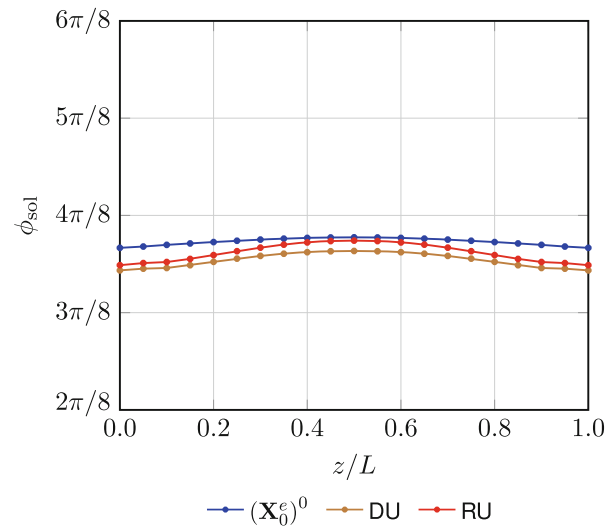
Fig. 28 A curved tube. Opening-angle comparison for the cutting location $\phi_c = \pi/2$, for the case $\phi = \pi/2$ and $\lambda_z = 1.2$
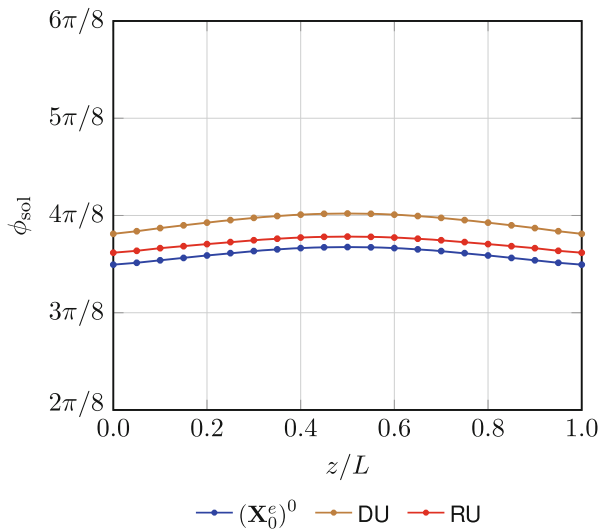
Fig. 27 A curved tube. Opening-angle comparison for the cutting location $\phi_c = \pi/2$, for the case $\phi = \pi/2$ and $\lambda_z = 1.0$

Fig. 29 A curved tube. Opening-angle comparison for the cutting location $\phi_c = \pi/2$, for the case $\phi = 5\pi/2$ and $\lambda_z = 1.0$

10^{-5}. In solving the steady-state structural mechanics equations for each iteration, the number of nonlinear iterations is 8, and the number of GMRES iterations per nonlinear iteration is 300. The number of iterations to obtain the converged solution for each case is given in Table 4.

We inspect the longitudinal prestretch, λ_z, as a function of η. As can be seen in Figs. 16, 17, 18 and 19, the prestretch introduced by $(\mathbf{X}_0^e)^0$ matches the specified prestretch very well. That is because the mapping that gives us $(\mathbf{X}_0^e)^0$, which is represented by Eq. (63), was designed with the objective to match the specified longitudinal prestretch. On the other hand, the prestretch introduced by $\mathbf{X}_0^e$, shown in Figs. 20, 21, 22 and 23, is close to the specified prestretch but does not

match it. That is because the objective in the iterations that give us $\mathbf{X}_0^e$ is to match the target shape.

4.2.2 LC state

The LC state for the arbitrary shape depends on the cutting location. We test three locations: $\theta_c = -\pi/2, 0, \pi/2$, which are shown in Fig. 24. We compute the LC state with the initial guess coming from the slit target shape, with zero pressure. We solve the structural mechanics problem based on the steady-state equations, using 288 nonlinear iterations. The number of GMRES iterations per nonlinear iteration is
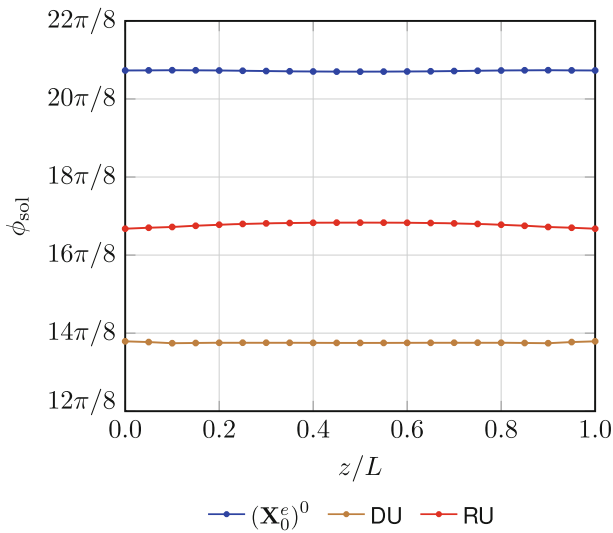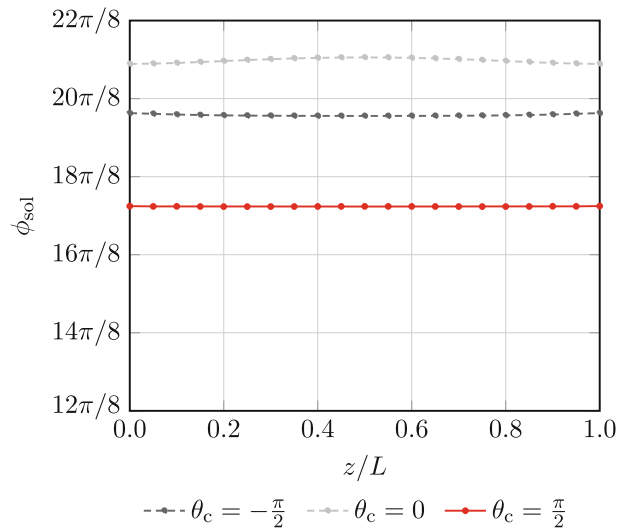
Fig. 30 A curved tube. Opening-angle comparison for the cutting location $\phi_c = \pi/2$, for the case $\phi = 5\pi/2$ and $\lambda_z = 1.2$
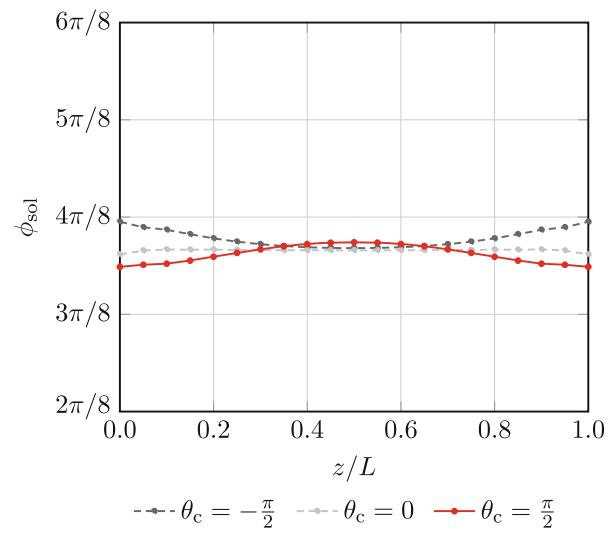
Fig. 32 A curved tube. Opening-angle comparison for all three cutting locations, for the case $\phi = \pi/2$ and $\lambda_z = 1.2$
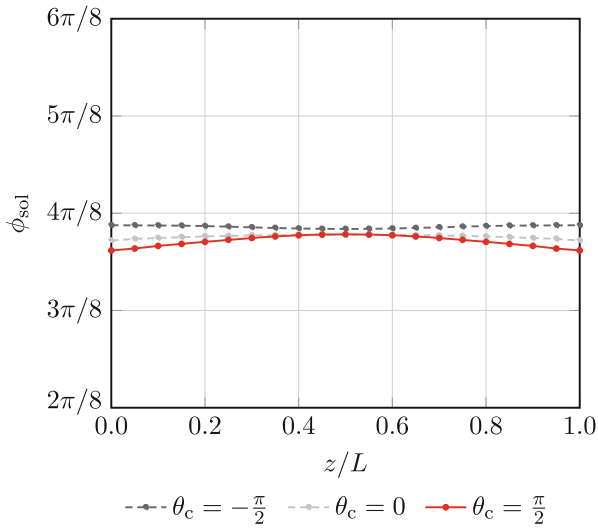
Fig. 31 A curved tube. Opening-angle comparison for all three cutting locations, for the case $\phi = \pi/2$ and $\lambda_z = 1.0$

Fig. 33 A curved tube. Opening-angle comparison for all three cutting locations, for the case $\phi = 5\pi/2$ and $\lambda_z = 1.0$

100 for the first 80 nonlinear iterations, 500 for the next 80, and 1,500 for the last 128.

Figures 25 and 26 show examples of the LC state. We compare the DU and RU processes by checking the opening angle as a function of z. For that, we define an opening angle for each layer of elements in the z direction. For each layer, the opening angle is calculated by summing the angles between the two faces of each column of elements in the thickness direction, and subtracting that from 2π. The unit vector associated with each face is calculated by area-weighted averaging of the unit vectors associated with the contributing element faces. Figures 27, 28, 29 and 30 show the opening angle for the cutting location $\theta_c = \pi/2$, obtained

from the ZS state given by $(\mathbf{X}_0^e)^0$ and by $\mathbf{X}_0^e$ computed with the DU and RU processes.

In evaluating the performance of the methods, the opening angle we are targeting is the one obtained from the ZS state given by $(\mathbf{X}_0^e)^0$. We note that, because of the mapping from $(\mathbf{X}_0^e)_T$ to $(\mathbf{X}_0^e)^0$, that opening angle cannot be expected to match the specified opening angle. As can be seen from Figures 27, 28, 29 and 30, the opening angle obtained from $\mathbf{X}_0^e$ computed with the RU process is closer to the target opening angle. Figures 31, 32, 33 and 34 show the opening angle for all three cutting locations.
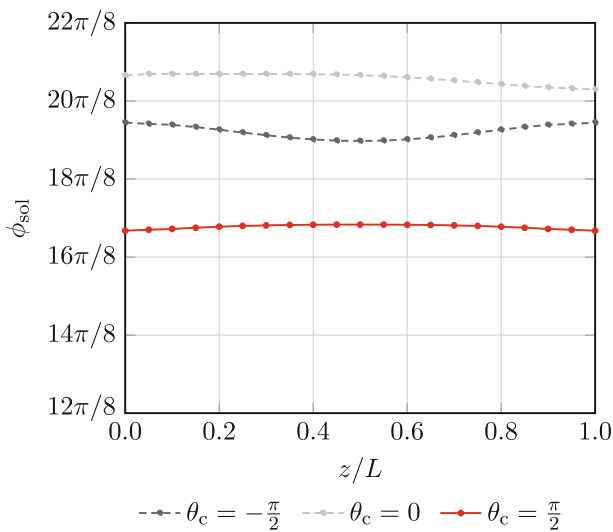
Fig. 34 A curved tube. Opening-angle comparison for all three cutting locations, for the case $\phi = 5\pi/2$ and $\lambda_z = 1.2$

5 Concluding remarks

We have presented a method for estimation of element-based ZS state in arterial FSI computations. Using the ZS state in the computations takes into account the fact that in patient-specific arterial FSI modeling the image-based arterial geometry comes from a configuration that is not stress-free. The method has three components. The first component is an iterative method, which iterates on the ZS state to match the image-based target shape for a given pressure load. The initial guess needed for the iterations is generated by the second component, which is a method for straight-tube geometries with single and multiple layers. The element-based ZS state for the straight tube is computed to match the given diameter and longitudinal stretch in the target configuration and the opening angle. The opening angle, which is related to the circumferential residual stress and treated as part of the given data, is measured by cutting the arterial wall open. The third component is an element-based mapping between the arterial and straight-tube configurations. It is for mapping from the arterial configuration to the straight-tube configuration, and for mapping the estimated ZS state of the straight tube back to the arterial configuration, so that it can be used as the initial guess for the iterative method that matches the image-based target shape. We carried out a number of test computations with the method to show how it works. The test computations were based on straight-tube configurations with single and three layers, and a curved-tube configuration with single layer. The test computations support our belief that we have a good method for estimation of element-based ZS state.

References

1. Torii R, Oshima M, Kobayashi T, Takagi K, Tezduyar TE (2004) Influence of wall elasticity on image-based blood flow simulation. Jpn Soc Mech Eng J Ser A 70:1224–1231 in Japanese
2. Torii R, Oshima M, Kobayashi T, Takagi K, Tezduyar TE (2006) Computer modeling of cardiovascular fluid–structure interactions with the deforming-spatial-domain/stabilized space–time formulation. Comput Methods Appl Mech Eng 195:1885–1895. doi:10.1016/j.cma.2005.05.050
3. Torii R, Oshima M, Kobayashi T, Takagi K, Tezduyar TE (2006) Fluid–structure interaction modeling of aneurysmal conditions with high and normal blood pressures. Comput Mech 38:482–490. doi:10.1007/s00466-006-0065-6
4. Bazilevs Y, Calo VM, Zhang Y, Hughes TJR (2006) Isogeometric fluid–structure interaction analysis with applications to arterial blood flow. Comput Mech 38:310–322
5. Tezduyar TE, Sathe S, Cragin T, Nanna B, Conklin BS, Pausewang J, Schwaab M (2007) Modeling of fluid–structure interactions with the space–time finite elements: arterial fluid mechanics. Int J Numer Methods Fluids 54:901–922. doi:10.1002/fld.1443
6. Torii R, Oshima M, Kobayashi T, Takagi K, Tezduyar TE (2007) Influence of wall elasticity in patient-specific hemodynamic simulations. Comput Fluids 36:160–168. doi:10.1016/j.compfluid.2005.07.014
7. Torii R, Oshima M, Kobayashi T, Takagi K, Tezduyar TE (2007) Numerical investigation of the effect of hypertensive blood pressure on cerebral aneurysm—dependence of the effect on the aneurysm shape. Int J Numer Methods Fluids 54:995–1009. doi:10.1002/fld.1497
8. Bazilevs Y, Calo VM, Tezduyar TE, Hughes TJR (2007) YZβ discontinuity-capturing for advection-dominated processes with application to arterial drug delivery. Int J Numer Methods Fluids 54:593–608. doi:10.1002/fld.1484
9. Tezduyar TE, Sathe S, Schwaab M, Conklin BS (2008) Arterial fluid mechanics modeling with the stabilized space–time fluid–structure interaction technique. Int J Numer Methods Fluids 57:601–629. doi:10.1002/fld.1633
10. Torii R, Oshima M, Kobayashi T, Takagi K, Tezduyar TE (2008) Fluid–structure interaction modeling of a patient-specific cerebral aneurysm: influence of structural modeling. Comput Mech 43:151–159. doi:10.1007/s00466-008-0325-8
11. Bazilevs Y, Calo VM, Hughes TJR, Zhang Y (2008) Isogeometric fluid–structure interaction: theory, algorithms, and computations. Comput Mech 43:3–37
12. Isaksen JG, Bazilevs Y, Kvamsdal T, Zhang Y, Kaspersen JH, Waterloo K, Romner B, Ingebrigtsen T (2008) Determination of wall tension in cerebral artery aneurysms by numerical simulation. Stroke 39:3172–3178
13. Tezduyar TE, Schwaab M, Sathe S (2009) Sequentially-coupled arterial fluid–structure interaction (SCAFSI) technique. Comput Methods Appl Mech Eng 198:3524–3533. doi:10.1016/j.cma.2008.05.024
14. Torii R, Oshima M, Kobayashi T, Takagi K, Tezduyar TE (2009) Fluid–structure interaction modeling of blood flow and cerebral aneurysm: significance of artery and aneurysm shapes. Comput Methods Appl Mech Eng 198:3613–3621. doi:10.1016/j.cma.2008.08.020
15. Bazilevs Y, Gohean JR, Hughes TJR, Moser RD, Zhang Y (2000) "Patient-specific isogeometric fluid–structure interaction analysis of thoracic aortic blood flow due to implantation of the Jarvik (2000) left ventricular assist device". Comput Methods Appl Mech Eng 198(2009):3534–3550
16. Bazilevs Y, Hsu M-C, Benson D, Sankaran S, Marsden A (2009) Computational fluid–structure interaction: methods and

application to a total cavopulmonary connection. Comput Mech 45:77–89

17. Takizawa K, Christopher J, Tezduyar TE, Sathe S (2010) Space–time finite element computation of arterial fluid–structure interactions with patient-specific data. Int J Numer Methods Biomed Eng 26:101–116. doi:10.1002/cnm.1241

18. Tezduyar TE, Takizawa K, Moorman C, Wright S, Christopher J (2010) Multiscale sequentially-coupled arterial FSI technique. Comput Mech 46:17–29. doi:10.1007/s00466-009-0423-2

19. Takizawa K, Moorman C, Wright S, Christopher J, Tezduyar TE (2010) Wall shear stress calculations in space–time finite element computation of arterial fluid–structure interactions. Comput Mech 46:31–41. doi:10.1007/s00466-009-0425-0

20. Torii R, Oshima M, Kobayashi T, Takagi K, Tezduyar TE (2010) Influence of wall thickness on fluid–structure interaction computations of cerebral aneurysms. Int J Numer Methods Biomed Eng 26:336–347. doi:10.1002/cnm.1289

21. Torii R, Oshima M, Kobayashi T, Takagi K, Tezduyar TE (2010) Role of 0D peripheral vasculature model in fluid–structure interaction modeling of aneurysms. Comput Mech 46:43–52. doi:10.1007/s00466-009-0439-7

22. Bazilevs Y, Hsu M-C, Zhang Y, Wang W, Liang X, Kvamsdal T, Brekken R, Isaksen J (2010) A fully-coupled fluid–structure interaction simulation of cerebral aneurysms. Comput Mech 46:3–16

23. Sugiyama K, Ii S, Takeuchi S, Takagi S, Matsumoto Y (2010) Full Eulerian simulations of biconcave neo-Hookean particles in a Poiseuille flow. Comput Mech 46:147–157

24. Bazilevs Y, Hsu M-C, Zhang Y, Wang W, Kvamsdal T, Hentschel S, Isaksen J (2010) Computational fluid–structure interaction: methods and application to cerebral aneurysms. Biomech Model Mechanobiol 9:481–498

25. Bazilevs Y, del Alamo JC, Humphrey JD (2010) From imaging to prediction: emerging non-invasive methods in pediatric cardiology. Prog Pediatr Cardiol 30:81–89

26. Takizawa K, Moorman C, Wright S, Purdue J, McPhail T, Chen PR, Warren J, Tezduyar TE (2011) Patient-specific arterial fluid–structure interaction modeling of cerebral aneurysms. Int J Numer Methods Fluids 65:308–323. doi:10.1002/fld.2360

27. Manguoglu M, Takizawa K, Sameh AH, Tezduyar TE (2011) Nested and parallel sparse algorithms for arterial fluid mechanics computations with boundary layer mesh refinement. Int J Numer Methods Fluids 65:135–149. doi:10.1002/fld.2415

28. Torii R, Oshima M, Kobayashi T, Takagi K, Tezduyar TE (2011) Influencing factors in image-based fluid–structure interaction computation of cerebral aneurysms. Int J Numer Methods Fluids 65:324–340. doi:10.1002/fld.2448

29. Tezduyar TE, Takizawa K, Brummer T, Chen PR (2011) Space–time fluid–structure interaction modeling of patient-specific cerebral aneurysms. Int J Numer Methods Biomed Eng 27:1665–1710. doi:10.1002/cnm.1433

30. Hsu M-C, Bazilevs Y (2011) Blood vessel tissue prestress modeling for vascular fluid–structure interaction simulations. Finite Elem Anal Des 47:593–599

31. Manguoglu M, Takizawa K, Sameh AH, Tezduyar TE (2011) A parallel sparse algorithm targeting arterial fluid mechanics computations. Comput Mech 48:377–384. doi:10.1007/s00466-011-0619-0

32. Takizawa K, Brummer T, Tezduyar TE, Chen PR (2012) A comparative study based on patient-specific fluid–structure interaction modeling of cerebral aneurysms. J Appl Mech 79:010908. doi:10.1115/1.4005071

33. Takizawa K, Bazilevs Y, Tezduyar TE (2012) Space–time and ALE-VMS techniques for patient-specific cardiovascular fluid–structure interaction modeling. Arch Comput Methods Eng 19:171–225. doi:10.1007/s11831-012-9071-3

34. Takizawa K, Schjodt K, Puntel A, Kostov N, Tezduyar TE (2012) Patient-specific computer modeling of blood flow in cerebral arteries with aneurysm and stent. Comput Mech 50:675–686. doi:10.1007/s00466-012-0760-4

35. Yao JY, Liu GR, Narmoneva DA, Hinton RB, Zhang Z-Q (2012) Immersed smoothed finite element method for fluid–structure interaction simulation of aortic valves. Comput Mech 50:789–804

36. Bazilevs Y, Takizawa K, Tezduyar TE (2013) Computational fluid–structure interaction: methods and applications. Wiley, New York

37. Bazilevs Y, Takizawa K, Tezduyar TE (2013) Challenges and directions in computational fluid–structure interaction. Math Models Methods Appl Sci 23:215–221. doi:10.1142/S0218202513400010

38. Takizawa K, Schjodt K, Puntel A, Kostov N, Tezduyar TE (2013) Patient-specific computational analysis of the influence of a stent on the unsteady flow in cerebral aneurysms. Comput Mech 51:1061–1073. doi:10.1007/s00466-012-0790-y

39. Long CC, Marsden AL, Bazilevs Y (2013) Fluid–structure interaction simulation of pulsatile ventricular assist devices. Comput Mech. doi:10.1007/s00466-013-0858-3

40. Esmaily-Moghadam M, Bazilevs Y, Marsden AL (2013) A new preconditioning technique for implicitly coupled multidomain simulations with applications to hemodynamics. Comput Mech. doi:10.1007/s00466-013-0868-1

41. Takizawa K, Tezduyar TE (2012) Space–time fluid–structure interaction methods. Math Models Methods Appl Sci 22:1230001. doi:10.1142/S0218202512300013

42. Tezduyar TE, Cragin T, Sathe S, Nanna B (2007) FSI computations in arterial fluid mechanics with estimated zero-pressure arterial geometry. In: Onate E, Garcia J, Bergan P, Kvamsdal T (eds) Marine 2007. CIMNE, Barcelona

43. Liu SQ, Fung YC (1989) Relationship between hypertension, hypertrophy, and opening angle of zero-stress state of arteries following aortic constriction. J Biomech Eng 111:325–335

44. Saini A, Berry C, Greenwald S (1995) Effect of age and sex on residual stress in the aorta. J Vasc Res 32:398–405

45. Matsumoto T, Tsuchida M, Sato M (1996) Change in intramural strain distribution in rat aorta due to smooth muscle contraction and relaxation. Am J Physiol 271:H1711–1716

46. Lu X, Zhao JB, Wang GR, Gregersen H, Kassab GS (2001) Remodeling of the zero-stress state of femoral arteries in response to flow overload. Am J Physiol Heart Circ Physiol 280:H1547–1559

47. Holzapfel GA, Sommer G, Auer M, Regitnig P, Ogden RW (2007) Layer-specific 3D residual deformations of human aortas with non-atherosclerotic intimal thickening. Ann Biomed Eng 35:530–545

48. Liu SQ, Fung YC (1988) Zero-stress states of arteries. J Biomech Eng 110:82–84

49. Delfino A, Stergiopulos N, Moore JE, Meister JJ (1997) Residual strain effects on the stress field in a thick wall finite element model of the human carotid bifurcation. J Biomech 30:777–786

50. Antiga L, Piccinelli M, Botti L, Ene-Iordache B, Remuzzi A, Steinman DA (2008) An image-based modeling framework for patient-specific computational hemodynamics. Med Biol Eng Comput 46:1097–1112

51. Huang H, Virmani R, Younis H, Burke AP, Kamm RD, Lee RT (2001) The impact of calcification on the biomechanical stability of atherosclerotic plaques. Circulation 103:1051–1056

52. Saad Y, Schultz M (1986) GMRES: a generalized minimal residual algorithm for solving nonsymmetric linear systems. SIAM J Sci Stat Comput 7:856–869